mater.scichina.com link.springer.com

Published online 27 July 2020 | https://doi.org/10.1007/s40843-020-1398-5
Sci China Mater 2021, 64(2): 318–328

High-performance aluminum-polyaniline battery based on the interaction between aluminum ion and –NH groups

Dandan Wang[1], Haoyu Hu[1], Yifei Liao[1], Dongqing Kong[1], Tonghui Cai[1], Xiuli Gao[2], Han Hu[2], Mingbo Wu[2], Qingzhong Xue[1,2], Zifeng Yan[1], Hao Ren[1*] and Wei Xing[1,2*]

ABSTRACT **Aluminum-ion batteries (AIBs) are a type of promising energy storage device due to their high capacity, high charge transfer efficiency, low cost, and high safety. However, the most investigated graphitic and metal dichalcogenide cathodes normally possess only a moderate capacity and a relatively low cycling stability, respectively, which limit the further development of high-performance AIBs. Here, based on the results of first principles calculations, we developed a polyaniline/graphene oxide composite that exhibited outstanding performances as a cathode material in AIBs (delivering 180 mA h g^{-1} after 4000 cycles), considering both the discharge capacity and the cycling performance. Ex-situ characterizations verified that the charge storage mechanism of polyaniline depended on the moderate interactions between –NH in the polyaniline chain and the electrolyte anions, such as $AlCl_4^-$. These findings lay the foundation of the development of high-performance AIBs based on conducting polymers.**

Keywords: first principles calculations, polyaniline, aluminum-ion batteries, energy storage mechanism

INTRODUCTION

In recent years, the high consumption of fossil fuels and the consequent environmental problems have promoted the rapid developments of solar, wind, tidal and other renewable energy [1,2]. The intermittent nature of renewable energy requires large-scale energy storage technologies to store energy before it is fed into the grid. Due to the high earth abundance, large theoretical capacity and high safety of aluminum, rechargeable aluminum-ion batteries (AIBs) as a large-scale energy storage device in the future have attracted extensive interest [3–6]. Traditional AIBs based on aqueous electrolyte are limited by aluminum anode corrosion and passivation film formation [7,8]. Recently, these limitations were overcome effectually by the introduction of room-temperature ionic liquid electrolytes (e.g., [EMIm]Cl/$AlCl_3$) [9]. Up to now, there are basically two types of cathode materials intensively investigated. One is the graphitic materials, such as natural graphite [10], graphite foam [11], graphene nanoflakes [12]. These materials present a limited capacity (usually less than 120 mA h g^{-1}) in storing large-size $AlCl_4^-$ (0.528 nm) [13] into the graphitic interlayer space. The other is metal dichalcogenides, such as transition metal oxides (V_2O_5 [14–16], VO_2 [17,18]), sulfides (SnS_2 [19], TiS_2 [20], MoS_2 [21,22], Mo_6S_8 [23,24], FeS_2 [25], CuS [26], NiS [27] or Ni_3S_2 [28]) and selenide ($CoSe_2$ [29]). Generally, the cyclic stability of these materials is rather poor due to the remarkable irreversibility of conversion reactions [26] or structural collapse induced by repeated ion insertion/de-insertion of complex ions, such as Al_xCl_y or Al cation [30].

Very recently, organic materials have emerged as a new type of promising cathode materials for AIBs. Walter *et al.* [31] developed an organic poly structure (nitropyrene-co-pyrene) with a storage capacity of 100 mA h g^{-1} and a high energy efficiency (86%) at 200 mA g^{-1} after 1000 cycles. Kim *et al.* [32] used redox-active phenanthrenequinone-based macrocycle compound/graphite flake composites, which presented a reversible capacity of 126 mA h g^{-1} through the insertion/de-insertion of chloroaluminate anions along with a superior lifetime of 500 cycles. The common feature of these two types of

[1] State Key Laboratory of Heavy Oil Processing, School of Material Science and Engineering, China University of Petroleum, Qingdao 266580, China
[2] Institute of New Energy, China University of Petroleum, Qingdao 266580, China
* Corresponding authors (emails: xingwei@upc.edu.cn (Xing W); renh@upc.edu.cn (Ren H))

organic materials is their conjugated feature.

Herein, we envisioned that conducting polymers, such as polyaniline (PANI), had long-range conjugated structure with the possibility of storing aluminum ions and merit of good electrical conductivity. The possiblity of using PANI as an AIB cathode was evaluated by the first principles calculations, suggesting that PANI was a promising candidate for the AIB cathode with the moderate electrostatic interaction between $[AlCl_4]^-$ and –NH group in the PANI chain. Guided by the first principles calculations, we *in-situ* synthesized PANI on the surface of graphene oxide (GO), resulting in a PANI/graphene oxide (G-PANI) composite. The original intention of using GO substrate was to evenly disperse PANI to expose more active sites. When evaluated as an AIB cathode, the G-PANI achieves a very high specific capacity (180 mA h g^{-1} at 1000 mA g^{-1}), good rate performance (155 mA h g^{-1} at 2000 mA g^{-1}), and excellent cycling stability with no capacity loss after 4000 cycles. Considering both the discharge capacity and cycle number, this performance is superior to most of the other cathode materials reported previously in AIBs.

EXPERIMENTAL SECTION

Theoretical calculations

Spin polarized first principles density functional theory (DFT) calculations were carried out to elucidate the storage mechanism of $[AlCl_4]^-$ in the PANI by using the DMol^3 package [33]. A periodic chain of PANI with a supercell consisting of 10 aniline units was set as the model PANI. All the amine nitrogen atoms were hydrogenated to represent the fully reduced leucoemeraldine state of PANI [34]. The DFT Semicore Pseudopotential, the Perdew-Burke-Ernzerhof cheme of function, and double numerical basis sets with polarization functions were employed to describe the nuclear-electron interactions, the exchange-correlation effects, and to expand the Kohn-Sham wavefunctions, respectively. The Tkatchenko-Scheffler dispersion correction was used to describe weak van der Walls interactions.

The supercell had a transverse size of 15×15 Å^2 perpendicular to the chain direction. All the atomic coordinates as well as the lattice constant along the chain direction were fully optimized with Γ-point-only electronic structure calculations. The real-space global cutoff radius was set to be 5.2 Å. The convergence tolerances for energy, force and displacement were set to 1×10^{-5} Ha, 0.02 Ha/Å, and 0.005 Å, respectively.

The n-th step-by-step binding energy was defined as the energy change upon the reaction

$$PANI[AlCl_4^-]_{n-1} + AlCl_4^- \rightarrow PANI[AlCl_4^-]_n. \quad (1)$$

And the corresponding average binding energy was given by the energetic effect of the reaction

$$PANI + nAlCl_4^- \rightarrow PANI[AlCl_4^-]_n, \quad (2)$$

divided by n.

The charge density difference was given by

$$\delta_\rho = \rho(PANI[AlCl_4^-]) - [\rho(PANI) + \rho(AlCl_4^-)], \quad (3)$$

where the three terms in the right hand side represent the total charge densities of the $AlCl_4^-$ binding to PANI, the PANI, and an isolated $AlCl_4^-$ ion, respectively.

Preparation of GO

The GO was prepared according to the modified Hummer's method [35,36]. A 9:1 mixture of H_2SO_4:H_3PO_4 (360:40 mL) was added to a mixture of graphite flakes (3.0 g, 1 wt% equiv.) and $KMnO_4$ (18.0 g, 6 wt% equiv.), causing a slightly exothermic reaction at 35–40°C. The reaction was then heated up to 50°C and the mixture was stirred for 12 h. Then, it was cooled down to room temperature and poured onto 400 mL of ice with 3 mL of 30% H_2O_2. The mixture was centrifuged at 7000 rpm for 5 min and the supernatant was discarded. The remaining solid was then washed in succession with 200 mL of water, 200 mL of 30% HCl solution, and 200 mL of ethanol. After each washing, the mixture was centrifuged at 7000 rpm for 10 min and the supernatant was discarded. The resulting solid was vacuum-dried overnight at room temperature to obtain GO.

Preparation of PANI/graphene oxide composite

A certain amount of GO was dispersed in 37.5 mL of deionized water and the mixture was sonicated for 30 min. Then, 4.2 mL of HCl was added and the mixture was stirred for another 30 min at 0°C. Afterwards, 0.8 mL of aniline and 8.3 mL of ammonium persulfate solution were added to the mixture and stirred vigorously for 24 h at 0°C. The suspension was then aged at 85°C for 72 h. The obtained product was filtered through a polyester fiber (Carpenter Co.) and washed with deionized water several times to remove the impurities. The wet product was then lyophilized and the dried compound was named G-PANI-x, where x represents the feed mass ratio between aniline and graphene. For comparison, pure PANI and GO aerogel (GOA) samples were also prepared by the same procedures except for the absence of GO or aniline, respectively. In a sense, GOA is a hydrothermally-treated GO at 85°C.

Ionic liquid electrolyte preparation

The ionic liquid electrolyte was prepared by slowly dis-

solving anhydrous aluminum chloride ($AlCl_3$) in 1-ethyl-3-methylimidazolium chloride ([EMIm]Cl) with a molar ratio of 1.3:1. The solution was stirred in an argon-atmosphere glove box ($[O_2]$ < 0.01 ppm, $[H_2O]$ < 0.01 ppm). Moreover, the ionic liquid electrolyte was maintained at 150°C under vacuum for 6 h and was left to cure for at least 12 h before using.

Materials characterizations

The microscopic morphology and the microstructure of the samples were observed *via* field-emission scanning electron microscopy (SEM, Sirion 200, FEI, Netherlands). The energy dispersive X-ray spectrometry (EDX) mapping of the samples was conducted by employing an INC 250 from Japan Electronic. The functional groups contained in the samples were probed by Fourier-transform infrared spectroscopy (FT-IR, Nicolet 6700, Thermo-scientific, USA). The sample crystal structures were analyzed *via* powder X-ray diffraction measurements (XRD, D8 Advance, Bruker, Germany) by using the CuKα radiation at 40 kV and 30 mA. The conductivity of powder samples was measured by powder resistivity instrument (SZT-D, ST2253, China) under the pressure of 40 MPa. X-ray photoelectron spectroscopy (XPS, PHI 5000 Versa Probe, ULVAC-PHI, Japan) performed with an Al Kα X-ray source (1486.6 eV) was used to study the surface chemical composition and the valent state of the elements. The Raman spectra were recorded by using a 532-nm laser excitation at room temperature (DXR, Thermo Fisher Scientific). The ^{27}Al nuclear magnetic resonance (NMR) spectra of the samples were measured on a Bruker Advance 400 spectrometer with a 1.0 mol L^{-1} $Al(NO_3)_3$ aqueous solution as the external chemical shift standard.

Fabrication of the electrochemical cell

The samples were ground with acetylene black and polyvinylidene fluoride (PVDF) with a mass ratio of 6:3:1 to prepare the cathodes. After adding methylpyrrolidone as the dispersing agent, the mixture was coated onto a rounded molybdenum current collector of 12 mm-diameter, which was dried at 80°C in vacuum for 12 h. The amount of the active material loaded was in the range of 1.5–2 mg. An aluminum foil (99.99%) was used as the anode. The AIBs were assembled by using a customized Swagelok-type cell in an argon-filled glove box at room temperature. One piece of glass fiber paper (Whatman 934-AH) was placed between the Al anode and the cathode. An aliquot (500 μL) of ionic liquid electrolyte was added to the cell to wet the separator.

Electrochemical measurements

The galvanostatic charge/discharge measurements were performed on a LANHE battery tester. The data of cycling performance was collected after stabilization for 300 cycles. Cyclic voltammetry (CV) measurements were conducted with different scan rates over a range of 0.1–2.4 V *versus* Al/$AlCl_4^-$ on an electrochemical workstation (CHI 660E, Chenhua Instrument Corporation, China) using a three-electrode mode, where the reference electrode was constituted of an Al strip, the counter electrode of an Al foil, and the working electrode of the samples, which were coated on a Mo foil.

RESULTS AND DISCUSSION

We first built a PANI model (a periodic chain with supercell of ten anilines) to evaluate its possibility of storing aluminum ions (e.g., $AlCl_4^-$) using first principles DFT calculations. The results show that the $AlCl_4^-$ binds to the PANI chain with two or three of its chlorine atoms approaching the two ortho-sites of the amine hydrogen atom, while different $AlCl_4^-$ ions are scattered along the two sides of the PANI chain to minimize the electrostatic repulsion (Fig. 1a–c). Fig. 1d shows the binding energy of $AlCl_4^-$ to PANI with varying $AlCl_4^-$ concentrations. It is shown that the average binding energy remains negative as the stoichiometric ratio between $AlCl_4^-$ and aniline units reaches 1:1, suggesting the combination of the $AlCl_4^-$ and PANI is thermodynamically spontaneous and implicates a theoretical capacity of 236 mA h g^{-1}. Furthermore, an average binding energy around −2.0 eV gives an estimated open circuit voltage of 2.0 V [37,38]. The charge density difference (Fig. 1e) further illustrates that $AlCl_4^-$ prefers binding to the hydrogen atom of –NH in the PANI chain *via* electrostatic interactions rather than forming chemical bonds. This electrostatic force-dominated interaction implies the $AlCl_4^-$ can easily attach to/detach from the PANI electrodes, potentially providing good rate performance.

The first principles predictions indicate that PANI is a good candidate of cathode material for AIBs with the working mechanism shown in Fig. 2a. To verify the results of first principles calculations, we *in-situ* synthesized PANI on the surface of GO, resulting in a G-PANI composite (Fig. 2b). For comparison, pure GOA and pure PANI were also prepared.

The morphology of the G-PANI-*x* was observed by SEM. As shown in Fig. 3a and Fig. S1a, GOA shows a three-dimensional network structure with folded and cross-linked GO sheets. With the addition of PANI, the corrugated nanosheets become gradually flat and thicker.

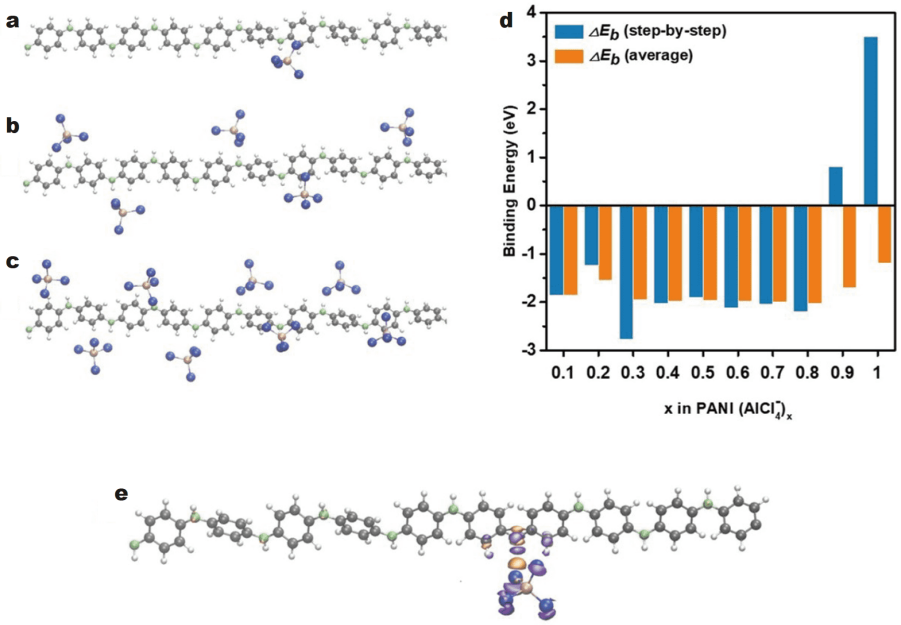

Figure 1 DFT optimized structures of PANI binding (a) 1, (b) 5, and (c) 8 $AlCl_4^-$; (d) binding energies of $AlCl_4^-$ to PANI with varying $AlCl_4^-$ concentrations (blue and orange bars represent step-by-step and average binding energies, respectively); (e) charge density difference upon a single $AlCl_4^-$ binding to PANI with orange and purple surfaces denoting the isosurfaces for electron accumulation and depletion, respectively (an isovalue of 0.015 a.u. was used).

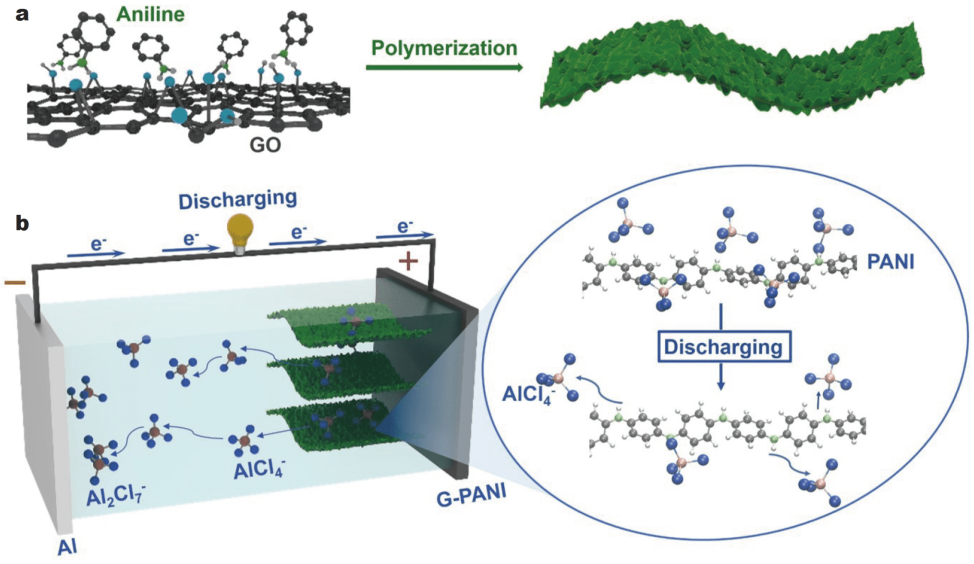

Figure 2 (a) Diagram of working mechanism for G-PANI-based AIBs; (b) schematic illustration for the preparation of the G-PANI composite.

This phenomenon may be related to the presence of PANI, which is adsorbed on the GO surface (Fig. S1b). When the amount of PANI is small, the material presents a single lamellar structure with a relatively smooth surface (as in the case of G-PANI-4). Upon the increase of the PANI content, the surface of the nanosheets is no longer smooth and some protrusions appear, which are typically observed in the morphology of loaded PANI (Fig. 3b and Fig. S1c) [39,40]. This peculiar morphology may enlarge the interface between PANI and the electrolyte. However, if too much PANI is present, the aggregation of the G-PANI nanosheets occurs, which may delay the infiltration

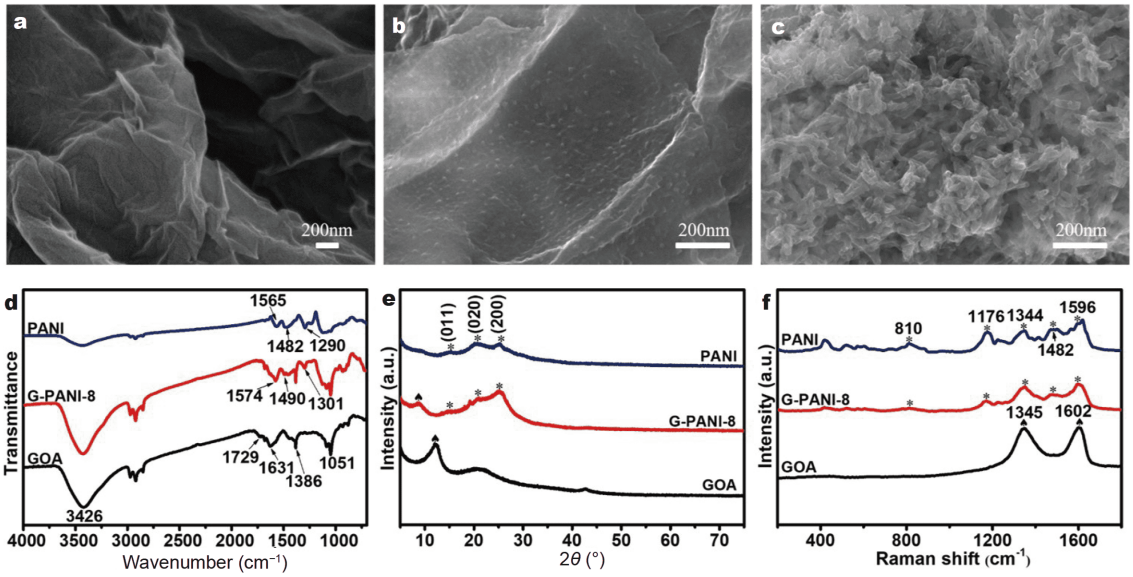

Figure 3 SEM images of (a) GOA, (b) G-PANI-8 and (c) PANI; (d) FT-IR spectra, (e) XRD patterns and (f) Raman spectra of the GOA, G-PANI-8 and PANI.

of the electrolyte (Fig. S1d). In contrast, the pure PANI presents nanorod shape with a diameter of around 20 nm (Fig. 3c).

The combination of GOA with PANI in the composite can be further verified *via* the FT-IR spectra shown in Fig. 3d. The FT-IR spectrum of GOA agrees with other previously reported results [41,42]. The absorption bands located at 3426 and 1729–1631 cm^{-1} indicate the stretching vibration of the –OH bond and of the C=O bond, respectively. The bands centered at 1386 and 1051 cm^{-1} are associated with the stretching vibration of the C–O bond, which is present in the C–OH/C–O–C groups. The C=N and C=C stretches of the quinonoid and benzenoid units of PANI are located at 1565 and 1482 cm^{-1}, respectively. In addition, a feature associated to the C–N stretch also appears at 1290 cm^{-1} [40,42]. The spectrum of the G-PANI-8 contains features of both GOA and PANI, indicating that these two constituents are successfully combined during the synthesis process. The bands located at 1565, 1482, and 1290 cm^{-1} are characteristic of the C=N, C=C, and C–N stretches of pure PANI. They blue shift to 1574, 1490, and 1301 cm^{-1}, respectively in the G-PANI-8, probably due to the π-π and hydrogen bonding interactions between GOA and PANI [43]. It is reported that the formation of π-π interaction and hydrogen bonding can effectively improve the electron conduction and structure stability of the composite [40,44]. Powder conductivity test reveals that the electrical conductivity of G-PANI-8 is apparently higher than those of pure PANI and GOA. (Table S1).

Fig. 3e shows the XRD patterns of the GOA, PANI, and G-PANI-8. The prominent peak, which is located at 2θ = 12.15°, is assigned to the [002] plane of GOA with a *d*-spacing of 0.728 nm. The spectrum of the G-PANI-8 shows three features at 2θ = 15.13°, 20.57°, and 25.17°, which correspond to the (011), (020), and (200) crystal planes of PANI, respectively [45]. Interestingly, the [002] peak of GOA in the G-PANI-8 presents a rather low intensity and shifts to 2θ = 8.73°. Its layer spacing is 1.01 nm, which suggests that the inter-planar spacing of GOA in the G-PANI-8 may be broaden due to the strong interactions between the GO sheet and PANI [42].

As shown in Fig. 3f, the Raman spectrum of GOA shows two prominent peaks at 1345 and 1602 cm^{-1}, which correspond to the D and G bands, respectively. For the Raman spectrum of G-PANI-8, apart from the D and G bands of GO, five new typical peaks generated by PANI can be found at 810, 1176, 1344, 1482 and 1596 cm^{-1}, which correspond to the substituted benzene ring deformation, C–H bending of the quinoid ring, C–N stretching, C=N stretching of the quinoid ring and C–C stretching of the benzoid, respectively [46,47]. Based on the analyses of the SEM data and the FT-IR, XRD, and Raman spectra, it is clear that the PANI and GO are well combined.

To evaluate the aluminium ion storage performance of the G-PANI composites, electrochemical measurements were conducted. The CV curve of the G-PANI-8 elec-

trode was scanned in the potential range of 0.1–2.4 V (Fig. 4a). A very prominent oxidation peak, corresponding to the reduction peak located at 0.9 V, is observed at 1.2 V. The CV curves recorded with various scan rates from 5 to 100 mV s^{-1} (Fig. 4a) possess similar redox couples. Moreover, the anodic and cathodic peaks gradually shift toward slightly positive and negative potentials, respectively, as the scan rate increases, indicating a weak polarization. These observations reveal that these redox reactions have an excellent kinetics. The relation between the peak current and the scan rates can be expressed *via* the following equations:

$$i = av^b, \quad (4)$$

$$\log i = \log a + b\log v, \quad (5)$$

where i is the response current (in mA) and v is the scan rate (in mV s^{-1}); a and b are adjustable values. As shown in the inset of Fig. 4a, b is close to a value of 0.732 for all the curves with a linear dependence. This suggests that the charge storage of G-PANI-8 is a combination of both a surface-controlled and a diffusion-controlled process. Fig. 4b and Fig. S2 further demonstrate that the surface-controlled charge storage increases gradually with the rise of scanning rate. The CV measurements are consistent with the galvanostatic charge-discharge curves (Fig. 4c). Obviously, there are a long and glossy voltage plateau (~1.0–2.0 V *vs.* Al/$AlCl_4^-$) in the charge process and a declined plateau (2.0–1.0 V *vs.* Al/$AlCl_4^-$) in the discharge process for G-PANI-8, which are not present for pure GOA. This process is related to the electrochemical redox reaction, which involves $[AlCl_4]^-$ and PANI.

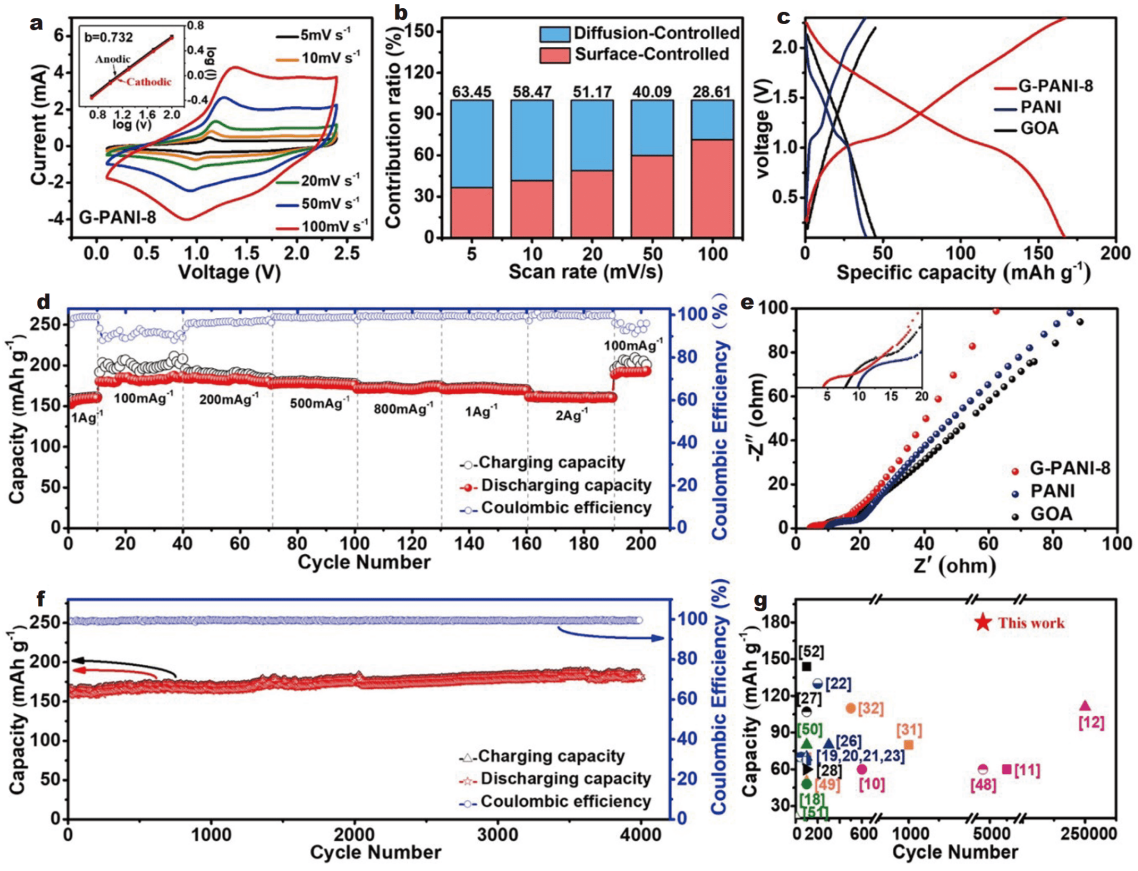

Figure 4 (a) Typical CV curves of the G-PANI-8 cathode at various scan rates from 5 to 100 mV s^{-1}; the inset shows the relation between the current and the scan rate; (b) contribution ratio of the surface-controlled charge of the G-PANI-8 electrode at different scan rates; (c) typical charge/discharge voltage profiles of the GOA, PANI and G-PANI-8 at a current density of 1000 mA g^{-1}; (d) specific capacities and coulombic efficiencies of the G-PANI-8 cathode at different current densities from 100 to 2000 mA g^{-1}; (e) Nyquist plots of the GOA, G-PANI-8 and PANI cathodes (the inset is the enlarged view of the high frequency region); (f) the cycling performance and the coulombic efficiency of the G-PANI-8 cathode at a current density of 1000 mA g^{-1} with the cut-off voltage of 2.3 V; (g) specific capacities and cyclic stability of metal-based, graphitic and organic cathode materials reported in AIBs (the pink dots represent graphitic materials [10–12,48], the orange dots represent organic materials [31,32,49], the green dots represent V-based materials [18,50,51], the black dots represent Ni-based materials [27,28,52] and the blue dots represent transition metal sulfides [19–23,26]).

Fig. 4d shows the rate performance of the G-PANI-8 cathode. The trend of the specific capacity and the coulombic efficiency of the cathode were monitored by altering the current density. The data show that the charge/discharge specific capacity of G-PANI-8 is almost independent from the current density. As the current density rises from 100 mA g^{-1} to 2 A g^{-1}, the specific capacity of the G-PANI-8 cathode only decreases 14.7%, exhibiting an excellent rate performance. This is consistent with the theoretical calculations. This excellent rate performance can be explained by the smaller ohmic resistance and charge-transfer resistance of G-PANI-8 (Fig. 4e and Fig. S3) [27,40]. The intersection of the curve with the *x*-axis in the high frequency region shows the ohmic resistance of the electrode. It is found that the ohmic resistance of G-PANI-8 is significantly lower than the value measured for pure GOA and PANI. This result is consistent with the results of powder conductivity test (Table S1). The higher conductivity of G-PANI-8 is expected to be due to the strong interactions between PANI and GO. The diameter of the half-ring in the high-frequency region is a key parameter of the charge transfer resistance of the electrode. It is found that the charge transfer resistance of G-PANI-8 shows the lowest value among the ensemble of samples investigated in this study. This can be explained by the high dispersion of the nano-sized PANI onto GO, which enables the ion doping/dedoping and redox reactions easier. Fig. 4f shows the cycling performance and the coulombic efficiency of the G-PANI-8 cathode. At a current density of 1 A g^{-1}, the discharge capacity almost stabilizes at 161 mA h g^{-1} with a coulombic efficiency of about 100% at a cut-off voltage of 2.3 V in the initial cycles. After 4000 cycles, the discharge capacity is fully retained and even shows slight increase to 180 mA h g^{-1}, which may be due to the improved access of anions into the PANI/graphene composite [53] and a slight reduction in the charge transfer resistance of the composite upon cycling (Fig. S4). This capacity is equivalent to x=0.6 in PANI$(AlCl_4^-)_x$ (Fig. 1d). The charge and discharge capacities are almost the same throughout these cycles, demonstrating the excellent reversibility of the G-PANI-*x* cathode. In contrast, when the cut-off voltage is lower than 2.3 V, the specific capacity of G-PANI-8 is reduced. Moreover, when the cut-off voltage is higher than 2.3 V, the coulombic efficiency is significantly lower and this may be attributed to the decomposition of the electrolyte under such a high voltage. Therefore, 2.3 V represents the optimized cut-off voltage for the G-PANI-8 cathode (Fig. S5). In addition, the composition and morphology of the material also have an impact on its electrochemical performances (Fig. S6). According to these results, the PANI/GO mass ratio of 8:1 is the optimal ratio to achieve the best electrochemical performance of the G-PANI-*x* composite. When the PANI content is too low, there are not enough redox active sites, thus reducing the specific capacity of the composite. As reflected by the SEM observations (Fig. 3a–c and Fig. S1), an excessive content of PANI results in the aggregation of the G-PANI-*x* nanosheets (as in the case of G-PANI-16), which lowers the infiltration of the electrolyte and the performances of the cathodes. The electrochemical performance of G-PANI-8 is superior to most of other state-of-the-art cathode materials previously reported (Fig. 4g and Table S2). The good performance is ascribed to four factors: (1) PANI is a highly active material to build AIB cathodes with a relatively high discharge potential; (2) the uniform dispersion of PANI on GO favours the efficient utilization of PANI active sites, which contributes to the high discharge capacity of the composite; (3) the uniform dispersion of PANI on GO and the strong interactions between them improve the electrical conductivity of the composite and enlarge the interface between PANI and the electrolyte, resulting in an good rate performance; (4) the nanosize of PANI and its strong interaction with GO generate a robust composite able to stand the repeated ion doping/dedoping with a super cycling stability.

To validate the energy-storage mechanism of PANI proposed by first principles calculations, a series of *ex-situ* measurements were carried out. The *ex-situ* XPS spectra and EDX were used to reveal the chemical state of the electrode in different charging/discharging states. As shown in Fig. 5a, the Al 2p and Cl 2p peaks are significantly more intense in the fully charged state than in the fully discharged state, indicating that the doping ions contain both Al and Cl elements. Furthermore, the EDX mapping of the charged/discharged samples (Fig. 5b, c and Table S3) reveals the Al and Cl are uniformly distributed over the G-PANI-8 cathode. Moreover, the Al and Cl signals increase simultaneously during the charging process, indicating the doping of $[AlCl_4]^-$. The remaining Al and Cl signals observed during the fully discharged state may be due to the irreversible incorporation of the Al and Cl species into the G-PANI-8 cathode.

XPS was further used to reveal the chemical state of the electrode in different charging/discharging states. Fig. 6a displays the N 1s spectra of G-PANI-8 in its fully charged and discharged states. These spectra can be deconvolved into four peaks with binding energies of 398.2, 398.8,

400.3, and 401.1 eV, which correspond to the =N–, –NH–, $–NH^{+}=$, and $–NH_2^{+}–$ species, respectively [54,55]. According to the peak area of the N atoms in different states, upon an increase in the cathode potential *versus* $Al/AlCl_4^-$ from 0.1 to 2.3 V, the binding energy of some N atoms decreases during the charge process. This is due to the fact that electron cloud density around the N atoms increases continuously as the $[AlCl_4]^-$ approaches –NH group, consistent with the simulated density distribution difference diagram (Fig. 1e). This process may prove the doping process of $[AlCl_4]^-$ into the G-PANI-8 cathode upon charging.

The ^{27}Al NMR spectra (Fig. 6b) show that the Al peak is significantly more intense in the fully charged state when compared with its fully discharged state, and this also indicate that $[AlCl_4]^-$ dopes into the PANI during the charge process. In addition, the Al peak located at 15 ppm shifts to 0 ppm during the charge process due to the strong interaction of $[AlCl_4]^-$ with the –NH groups in the PANI chain [25,56]. In the Raman spectra, the characteristic peaks of the G-PANI-8 composite decrease in intensity upon the increase in the cathode potential (Fig. 6c). When the cathode is charged up to 2.3 V, the peak intensities of PANI are substantially reduced. This can be explained by the uneven distribution of the electron cloud in the PANI chain with the doped $[AlCl_4]^-$, which may cause an increase in the polarity of some chemical bonds (e.g., C–N and C=N) and a decrease in the Raman peak intensity. In addition, the C–N stretch and the C=N stretch of the quinoid ring located at 1344 and 1482 cm^{-1} blue shift to 1349 and 1495 cm^{-1}, respectively, at the fully charged state. This observation is consistent with the simulated Raman spectra (Fig. 6d), which demonstrate that the intensity of the peaks is

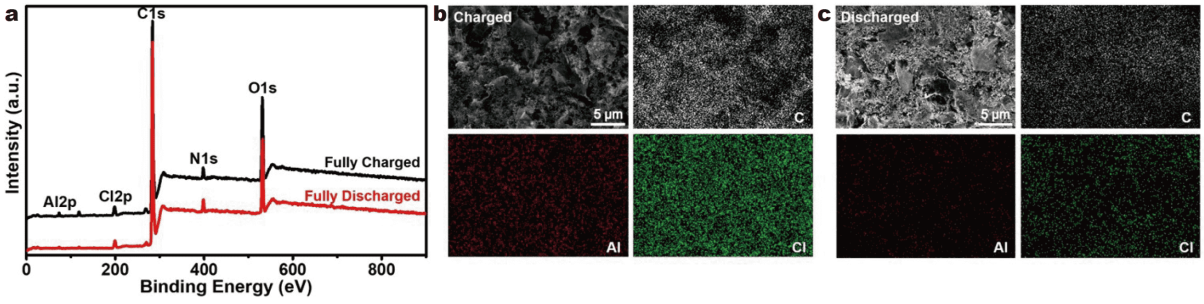

Figure 5 (a) *Ex-situ* XPS spectra of the G-PANI-8 cathode in different states; EDX mapping images for Al, Cl and C of the G-PANI-8 cathode (containing carbon black and PVDF) in (b) charged states and (c) discharged states.

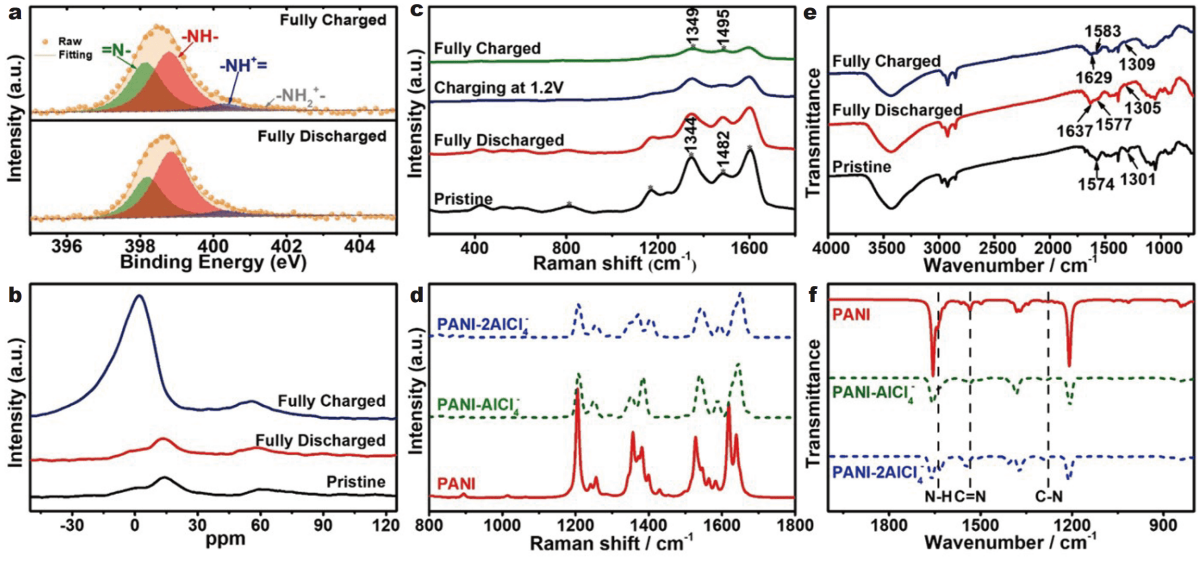

Figure 6 (a) *Ex-situ* XPS data of the N 1s peaks, (b) ^{27}Al NMR spectra (c) Raman of the G-PANI-8 cathode in different states; (d) Raman spectra of PANI and $AlCl_4$-doped PANI calculated by DFT-GGA; (e) FT-IR of the G-PANI-8 cathode in different states; (f) FT-IR spectra of PANI and $AlCl_4$-doped PANI calculated by DFT-GGA.

weaker and shows a clear blue-shift effect upon the incorporation of $AlCl_4^-$ into PANI. In the FT-IR spectra (Fig. 6e), the C=N and C–N peaks appear to blue-shift from 1574 to 1583 cm^{-1} and from 1301 to 1309 cm^{-1}, respectively. This trend is also consistent with the simulated FT-IR results (Fig. 6f). Furthermore, the red-shift of the N–H peak from 1637 to 1629 cm^{-1} can be associated with the decrease of both the binding energy of N and the bond energy of N–H as the $[AlCl_4]^-$ approaches the –NH group. [43,54] This agrees well with the XPS analyses (Fig. 6a).

Based on the first principles calculations and experimental data, the energy storage mechanism for PANI is proposed in Scheme S1. The cathode reaction can be illustrated as follows:

$$\text{Charging: PANI} + nX^- - ne^- \rightarrow \text{PANI}^{n+}(X^-)_n, \quad (6)$$

$$\text{Discharging: PANI}^{n+}(X^-)_n + ne^- \rightarrow \text{PANI} + nX^-, \quad (7)$$

where X^- represents $[AlCl_4]^-$. Here, $[AlCl_4]^-$ is assumed to be the only doping species. However, this assumption may be too restrictive since the electrolyte also contains $Al_2Cl_7^-$ and free Cl^- [57,58], which suggests that the doping of $Al_2Cl_7^-$ and free Cl^- into the PANI may also take place.

CONCLUSIONS

In summary, first principles calculations suggest that PANI is potentially a good candidate for the AIB cathode *via* the moderate electrostatic interaction between $[AlCl_4]^-$ and –NH group in the PANI chain. Inspired by this calculation results, we prepared the G-PANI composite that exhibits outstanding performance (a discharge capacity of 180 mA h g^{-1} at 1000 mA g^{-1} after 4000 cycles with the coulombic efficiency of around 100%). Considering both the discharge capacity and the number of cycles, the G-PANI prepared herein surpasses most of other reported cathode materials. *Ex-situ* characterizations proved the charge storage mechanism proposed by the first principles calculations. We believe that the methodology, materials and new understanding obtained in this work would be of great significance for the further development of AIBs based on the conjugated conducting polymers.

Received 25 March 2020; accepted 17 May 2020; published online 27 July 2020

1 Whittingham MS. Ultimate limits to intercalation reactions for lithium batteries. Chem Rev, 2014, 114: 11414–11443
2 Armand M, Tarascon JM. Building better batteries. Nature, 2008, 451: 652–657
3 Elia GA, Marquardt K, Hoeppner K, *et al.* An overview and future perspectives of aluminum batteries. Adv Mater, 2016, 28: 7564–7579
4 Li Q, Bjerrum NJ. Aluminum as anode for energy storage and conversion: a review. J Power Sources, 2002, 110: 1–10
5 Canepa P, Sai Gautam G, Hannah DC, *et al.* Odyssey of multivalent cathode materials: Open questions and future challenges. Chem Rev, 2017, 117: 4287–4341
6 Ambroz F, Macdonald TJ, Nann T. Trends in aluminium-based intercalation batteries. Adv Energy Mater, 2017, 7: 1602093
7 Sargent, DE. Voltaic cell. US Patent, 1951, 2554447
8 Holleck GL, Giner J. The aluminum electrode in $AlCl_3$-alkali-halide melts. J Electrochem Soc, 1972, 119: 1161–1166
9 Jayaprakash N, Das SK, Archer LA. The rechargeable aluminum-ion battery. Chem Commun, 2011, 47: 12610–12612
10 Wang DY, Wei CY, Lin MC, *et al.* Advanced rechargeable aluminium ion battery with a high-quality natural graphite cathode. Nat Commun, 2017, 8: 14283
11 Lin MC, Gong M, Lu B, *et al.* An ultrafast rechargeable aluminium-ion battery. Nature, 2015, 520: 324–328
12 Chen H, Xu H, Wang S, *et al.* Ultrafast all-climate aluminum-graphene battery with quarter-million cycle life. Sci Adv, 2017, 3: eaao7233
13 Jung SC, Kang YJ, Yoo DJ, *et al.* Flexible few-layered graphene for the ultrafast rechargeable aluminum-ion battery. J Phys Chem C, 2016, 120: 13384–13389
14 Wang H, Bai Y, Chen S, *et al.* Binder-free V_2O_5 cathode for greener rechargeable aluminum battery. ACS Appl Mater Interfaces, 2015, 7: 80–84
15 Gu S, Wang H, Wu C, *et al.* Confirming reversible Al^{3+} storage mechanism through intercalation of Al^{3+} into V_2O_5 nanowires in a rechargeable aluminum battery. Energy Storage Mater, 2017, 6: 9–17
16 Reed LD, Menke E. The roles of V_2O_5 and stainless steel in rechargeable Al–ion batteries. J Electrochem Soc, 2013, 160: A915–A917
17 Kulish VV, Manzhos S. Comparison of Li, Na, Mg and Al-ion insertion in vanadium pentoxides and vanadium dioxides. RSC Adv, 2017, 7: 18643–18649
18 Jiang J, Li H, Huang J, *et al.* Investigation of the reversible intercalation/deintercalation of Al into the novel Li_3VO_4@C microsphere composite cathode material for aluminum-ion batteries. ACS Appl Mater Interfaces, 2017, 9: 28486–28494
19 Hu Y, Luo B, Ye D, *et al.* An innovative freeze-dried reduced graphene oxide supported SnS_2 cathode active material for aluminum-ion batteries. Adv Mater, 2017, 29: 1606132
20 Geng L, Scheifers JP, Fu C, *et al.* Titanium sulfides as intercalation-type cathode materials for rechargeable aluminum batteries. ACS Appl Mater Interfaces, 2017, 9: 21251–21257
21 Li Z, Niu B, Liu J, *et al.* Rechargeable aluminum-ion battery based on MoS_2 microsphere cathode. ACS Appl Mater Interfaces, 2018, 10: 9451–9459
22 Yang W, Lu H, Cao Y, *et al.* Flexible free-standing MoS_2/carbon nanofibers composite cathode for rechargeable aluminum-ion batteries. ACS Sustain Chem Eng, 2019, 7: 4861–4867
23 Geng L, Lv G, Xing X, *et al.* Reversible electrochemical intercalation of aluminum in Mo_6S_8. Chem Mater, 2015, 27: 4926–4929
24 Mei L, Xu J, Wei Z, *et al.* Chevrel phase Mo_6T_8 (T = S, Se) as electrodes for advanced energy storage. Small, 2017, 13: 1701441
25 Mori T, Orikasa Y, Nakanishi K, *et al.* Discharge/charge reaction mechanisms of FeS_2 cathode material for aluminum rechargeable

batteries at 55°C. J Power Sources, 2016, 313: 9–14
26 Wang S, Jiao S, Wang J, *et al.* High-performance aluminum-ion battery with CuS@C microsphere composite cathode. ACS Nano, 2017, 11: 469–477
27 Yu Z, Kang Z, Hu Z, *et al.* Hexagonal NiS nanobelts as advanced cathode materials for rechargeable Al-ion batteries. Chem Commun, 2016, 52: 10427–10430
28 Wang S, Yu Z, Tu J, *et al.* A novel aluminum-ion battery: Al/$AlCl_3$-[EMIm]Cl/Ni_3S_2@graphene. Adv Energy Mater, 2016, 6: 1600137
29 Cai T, Zhao L, Hu H, *et al.* Stable $CoSe_2$/carbon nanodice@reduced graphene oxide composites for high-performance rechargeable aluminum-ion batteries. Energy Environ Sci, 2018, 11: 2341–2347
30 Tian H, Zhang S, Meng Z, *et al.* Rechargeable aluminum/iodine battery redox chemistry in ionic liquid electrolyte. ACS Energy Lett, 2017, 2: 1170–1176
31 Walter M, Kravchyk KV, Böfer C, *et al.* Polypyrenes as high-performance cathode materials for aluminum batteries. Adv Mater, 2018, 30: 1705644
32 Kim DJ, Yoo DJ, Otley MT, *et al.* Rechargeable aluminium organic batteries. Nat Energy, 2019, 4: 51–59
33 Delley B. From molecules to solids with the $DMol^3$ approach. J Chem Phys, 2000, 113: 7756–7764
34 Feast WJ, Tsibouklis J, Pouwer KL, *et al.* Synthesis, processing and material properties of conjugated polymers. Polymer, 1996, 37: 5017–5047
35 Hummers Jr. WS, Offeman RE. Preparation of graphitic oxide. J Am Chem Soc, 1958, 80: 1339
36 Marcano DC, Kosynkin DV, Berlin JM, *et al.* Improved synthesis of graphene oxide. ACS Nano, 2010, 4: 4806–4814
37 Van der Ven A, Deng Z, Banerjee S, *et al.* Rechargeable alkali-ion battery materials: theory and computation. Chem Rev, 2020
38 Chen T, Sai Gautam G, Huang W, *et al.* First-principles study of the voltage profile and mobility of Mg intercalation in a chromium oxide spinel. Chem Mater, 2018, 30: 153–162
39 Kumar NA, Choi HJ, Shin YR, *et al.* Polyaniline-grafted reduced graphene oxide for efficient electrochemical supercapacitors. ACS Nano, 2012, 6: 1715–1723
40 Wang L, Ye Y, Lu X, *et al.* Hierarchical nanocomposites of polyaniline nanowire arrays on reduced graphene oxide sheets for supercapacitors. Sci Rep, 2013, 3: 3568
41 Zhang WL, Park BJ, Choi HJ. Colloidal graphene oxide/polyaniline nanocomposite and its electrorheology. Chem Commun, 2010, 46: 5596–5598
42 Xu J, Wang K, Zu SZ, *et al.* Hierarchical nanocomposites of polyaniline nanowire arrays on graphene oxide sheets with synergistic effect for energy storage. ACS Nano, 2010, 4: 5019–5026
43 Wang H, Hao Q, Yang X, *et al.* Graphene oxide doped polyaniline for supercapacitors. Electrochem Commun, 2009, 11: 1158–1161
44 Luo Y, Guo R, Li T, *et al.* Application of polyaniline for Li-ion batteries, lithium-sulfur batteries, and supercapacitors. ChemSusChem, 2019, 12: 1591–1611
45 Yan J, Wei T, Shao B, *et al.* Preparation of a graphene nanosheet/polyaniline composite with high specific capacitance. Carbon, 2010, 48: 487–493
46 Yan X, Chen J, Yang J, *et al.* Fabrication of free-standing, electrochemically active, and biocompatible graphene oxide–polyaniline and graphene–polyaniline hybrid papers. ACS Appl Mater Interfaces, 2010, 2: 2521–2529
47 Wang H, Hao Q, Yang X, *et al.* Effect of graphene oxide on the properties of its composite with polyaniline. ACS Appl Mater Interfaces, 2010, 2: 821–828
48 Wu Y, Gong M, Lin MC, *et al.* 3D graphitic foams derived from chloroaluminate anion intercalation for ultrafast aluminum-ion battery. Adv Mater, 2016, 28: 9218–9222
49 Hudak NS. Chloroaluminate-doped conducting polymers as positive electrodes in rechargeable aluminum batteries. J Phys Chem C, 2014, 118: 5203–5215
50 Zhang X, Wang S, Tu J, *et al.* Flower-like vanadium suflide/reduced graphene oxide composite: an energy storage material for aluminum-ion batteries. ChemSusChem, 2018, 11: 709–715
51 Suto K, Nakata A, Murayama H, *et al.* Electrochemical properties of Al/vanadium chloride batteries with $AlCl_3$-1-ethyl-3-methylimidazolium chloride electrolyte. J Electrochem Soc, 2016, 163: A742–A747
52 Li S, Tu J, Zhang GH, Wang M, Jiao S. $NiCo_2S_4$ nanosheet with hexagonal architectures as an advanced cathode for Al-ion batteries. J Electrochem Soc, 2018, 165: A3504–A3509
53 Ai W, Luo Z, Jiang J, *et al.* Nitrogen and sulfur codoped graphene: multifunctional electrode materials for high-performance Li-ion batteries and oxygen reduction reaction. Adv Mater, 2014, 26: 6186–6192
54 Mi H, Li F, He C, *et al.* Three-dimensional network structure of silicon-graphene-polyaniline composites as high performance anodes for lithium-ion batteries. Electrochim Acta, 2016, 190: 1032–1040
55 Viswanathan A, Shetty AN. Single step synthesis of rGO, copper oxide and polyaniline nanocomposites for high energy supercapacitors. Electrochim Acta, 2018, 289: 204–217
56 Mroué KH, Emwas AHM, Power WP. Solid-state ^{27}Al nuclear magnetic resonance investigation of three aluminum-centered dyes. Can J Chem, 2010, 88: 111–123
57 Zhang M, Kamavarum V, Reddy RG. New electrolytes for aluminum production: ionic liquids. JOM, 2003, 55: 54–57
58 Jiang T, Chollier Brym MJ, Dubé G, *et al.* Electrodeposition of aluminium from ionic liquids: Part I—Electrodeposition and surface morphology of aluminium from aluminium chloride ($AlCl_3$)–1-ethyl-3-methylimidazolium chloride ([EMIm]Cl) ionic liquids. Surf Coat Tech, 2006, 201: 1–9

Acknowledgements This work was financially supported by the National Natural Science Foundation of China (51877216 and 21773309), Taishan Scholar Foundation (tsqn20161017), the Major Program of Shandong Province Natural Science Foundation (ZR201801280009), and the Fundamental Research Funds for the Central Universities (18CX05007A, 19CX05001A and 19CX05002A).

Author contributions Wang D performed the experiments and drafted the manuscript. Hu H and Liao Y plotted and checked the figures. Kong D and Cai T performed the sample characterizations. Gao X, Hu H and Wu M conducted the electrochemical assessment of the samples and *ex-situ* studies. Xue Q and Yan Z performed the theoretical calculations. Xing W and Ren H guided the idea and finalized the manuscript. All authors read and approved the final manuscript.

Conflict of interest The authors declare no conflict of interest.

Supplementary information Experimental details and supporting data are available in the online version of the paper.

Dandan Wang is a PhD candidate in the School of Material Science and Engineering at China University of Petroleum. She received her bachelor degree in chemical engineering from Shandong University of Technology. Her current research mainly focuses on the fabrication of polymer materials and the applications of aluminum ion batteries.

Wei Xing received his PhD degdree in chemical engineering from China University of Petroleum in 2005 under the co-supervision of Prof. Zifeng Yan and Prof. G.Q. Max Lu. After seven years of research and teaching at Shandong University of Technology, he joined China University of Petroleum as a full professor in December 2012. His research interests cover the functional materials for energy storage, CO_2 capture, and heterogeneous catalysis.

Hao Ren received his PhD in physical chemistry from the University of Science and Technology of China in 2010 under the supervision of Prof. Jinlong Yang, and another PhD in biotechnology from the Royal Institute of Technology, Sweden under the supervision of Prof. Yi Luo. He is currently an associated professor at China University of Petroleum. His current research mainly focuses on the development of *ab-initio* and machine learning methods for molecular spectroscopy.

基于铝离子与–NH基团相互作用的高性能铝-聚苯胺电池

王丹丹[1], 胡皓宇[1], 廖逸飞[1], 孔冬青[1], 蔡同辉[1], 高秀丽[2], 胡涵[2], 吴明铂[2], 薛庆忠[1,2], 阎子峰[1], 任浩[1*], 邢伟[1,2*]

摘要 铝离子电池作为一种高容量、高电荷转移率、低成本和高安全性的储能器件具有良好的应用前景. 但是, 阴极材料的电化学性能限制了铝离子电池的进一步发展, 例如目前研究最多的石墨类电极材料容量较低, 而过渡金属氧族化合物电极材料的循环稳定性相对较差. 本论文根据第一性原理的计算结果, 开发出一种聚苯胺/氧化石墨烯复合材料, 该复合材料作为铝离子电池阴极材料表现出极为出色的电化学性能(4000次循环后比容量依然能维持180 mA h g^{-1}). 多种非原位表征实验证明, 在充电过程中聚苯胺通过其–NH基团与电解质阴离子(如$AlCl_4^-$)之间的适度相互作用进行电荷存储. 本研究为基于导电聚合物正极材料的高性能铝离子电池的发展奠定了基础.

